

In-Situ Spectro-Electrochemistry of Conductive Polymers Using Plasmonics to Reveal Doping Mechanisms

Jialong Peng,[#] Qianqi Lin,[#] Tamás Földes, Hyeon-Ho Jeong, Yuling Xiong, Charalampos Pitsalidis, George G. Malliaras, Edina Rosta, and Jeremy J. Baumberg*



Cite This: <https://doi.org/10.1021/acsnano.2c09081>



Read Online

ACCESS |

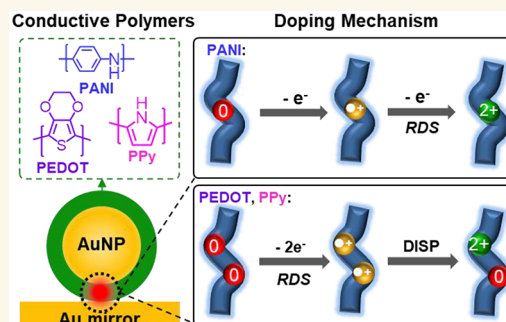
Metrics & More

Article Recommendations

Supporting Information

ABSTRACT: Conducting polymers are a key component for developing wearable organic electronics, but tracking their redox processes at the nanoscale to understand their doping mechanism remains challenging. Here we present an *in-situ* spectro-electrochemical technique to observe redox dynamics of conductive polymers in an extremely localized volume (<100 nm³). Plasmonic nanoparticles encapsulated by thin shells of different conductive polymers provide actively tuned scattering color through switching their refractive index. Surface-enhanced Raman scattering in combination with cyclic voltammetry enables detailed studies of the redox/doping process. Our data intriguingly show that the doping mechanism varies with polymer conductivity: a disproportionation mechanism dominates in more conductive polymers, while sequential electron transfer prevails in less conductive polymers.

KEYWORDS: conductive polymers, redox, doping mechanism, spectro-electrochemistry, plasmonics, nanoparticle, surface-enhanced Raman scattering



Conductive polymer thin films underpin advances in organic electronics due to their low-cost fabrication compared to silicon counterparts and their mechanical flexibility compatible with foldable devices.¹ The reversible doping/dedoping of conductive polymers is the basis of organic thin-film transistors,^{2,3} sensors,⁴ and displays.^{5,6} Doping transfers electrons in/out (i.e., reduction/oxidation) of the neutral conductive polymers, creating negative/positive charge carriers.^{7,8} Two-electron transfers are involved in generating polarons or bipolarons. The former contain monoradical ions (P^{•-} or P^{•+}), and the latter contain dianions/cations (P²⁻ or P²⁺). Although many techniques have been used to characterize the doping/redox process, conflicting conclusions often arise from the difficulty in obtaining a well-defined electrochemical response from the polymers, and it is unclear why short-lived polaron intermediates are sometimes observed but sometimes not.^{9–12} Understanding of the doping/redox mechanism is thus scarce, limiting development of widespread polymer-based applications.

A promising technique to address this challenge integrates such polymers into nanocavities, where their optical and vibrational properties can be interrogated in real time. By using plasmonic nanocavities which support optical hotspots in the nanogap between coinage metal components, the light can be

confined to nanoscale volumes of the polymer, while simultaneously electrons are transported only a few nanometers from these metal contacts (hence, this is rapid). We thus coat thin films of conductive polymers around gold nanoparticles (Au NPs) which are drop-cast onto a gold substrate, forming an electrochromic nanoparticle-on-mirror (eNPoM, Figure 1a) geometry. Such a plasmonic geometry has a well-defined electrochemical response^{5,6} and yields fast-switching color dynamics at the single-nanoparticle level. However, dark-field spectroscopy gives too little information for mechanistic studies seeking to identify the intermediates involved in the complex two-electron transfers. Surface-enhanced Raman spectroscopy (SERS), in combination with cyclic voltammetry, is a powerful technique to uncover structural fingerprints at the few-molecule level during redox transitions.¹³ Exploiting the NPoM geometry which supports highly confined optical fields

Received: September 12, 2022

Accepted: November 28, 2022

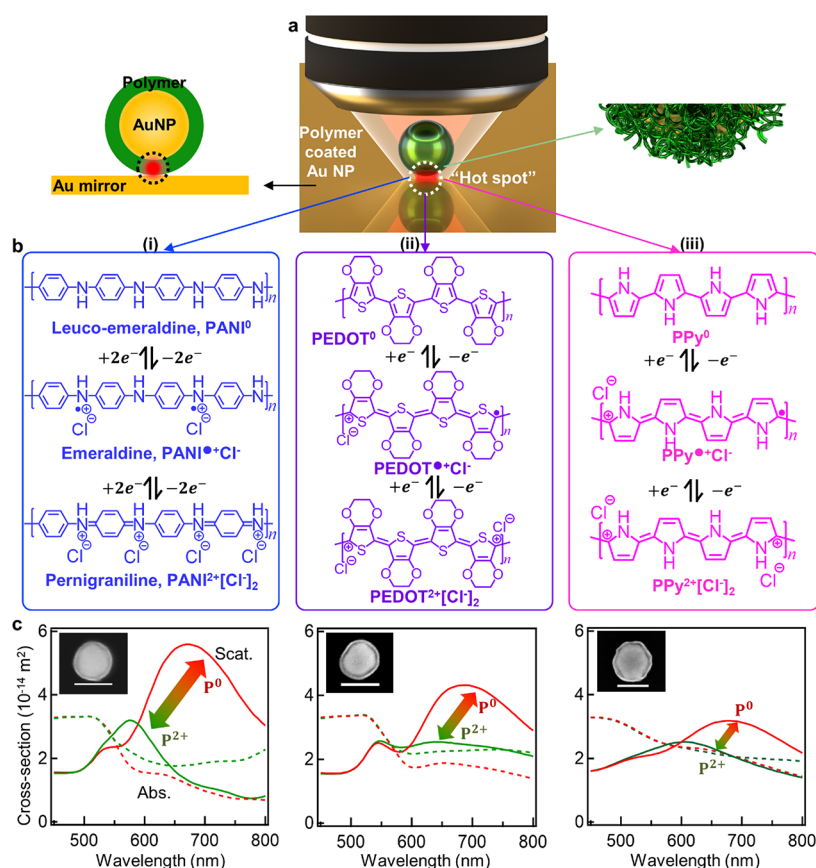


Figure 1. Conductive polymer redox in plasmonic hotspots. (a) Schematic of electrochromic nanoparticle-on-mirror (eNPoM). Each gold nanoparticle (Au NP) is coated with (i) polyaniline (Au@PANI), (ii) poly-3,4-ethylenedioxythiophene (Au@PEDOT), or (iii) polypyrrole (Au@PPy). Insets: cross-section of eNPoM (left) and zoom-in view of coated nanoparticle (right). (b) Redox polymer reactions (P^0 , reduced; $P^{\bullet+}$, intermediate; P^{2+} , oxidized), represented in tetramers with n repeat units. (c) Finite-difference time-domain (FDTD) simulated absorption (dashed) and scattering (line) spectra of individual eNPoMs for P^0 and P^{2+} states. Insets: scanning electron microscopic (SEM) images showing the core-shell structure. Au NP diameter is 80 nm, polymer thickness is 20 nm, and scale bar is 100 nm.

in the plasmonic hotspot gives a vibrational Raman scattering enhancement of $>10^4$. This technique thus allows *in situ* study of the thin-film conductive polymer redox in real time to reveal features of the doping mechanism.

We initially demonstrate reversible color switching of such eNPoMs using dark-field (DF) spectroscopy on Au NPs coated with either polyaniline (Au@PANI), poly-3,4-ethylenedioxythiophene (Au@PEDOT), or polypyrrole (Au@PPy). These are deposited around Au NPs in solution using surfactant-assisted chemical oxidative polymerization (Figure 1c insets) to 20 nm thickness for all data shown here (see Methods). The observed color dynamics in plasmonic scattering (Figure 1c) is a result of redox-induced changes in the molecular electronic transitions (Figure 1b), leading to changes in absorption and refractive index.^{14–16} *In-situ* surface-enhanced Raman spectroscopy is then used to probe the molecular vibronic changes during redox. The tight optical field confinement within individual plasmonic nanocavities gives high signal-to-noise ratios, allowing a spectro-electrochemical study of conductive polymers during redox down to volumes $\sim(20 \text{ nm})^3$.

RESULTS AND DISCUSSION

eNPoM Optical Switching. To track the conductive polymer redox optically, customized spectro-electrochemical cells with three electrodes are used to control the shell polymer redox state (see Methods and Supporting Information (SI

Figure S1). All three polymers can undergo $2e^-$ transfers resulting in three redox states (Figure 1b), with appropriate electrolytes (see Methods). Finite-difference time-domain (FDTD) simulations of the optical scattering spectra (Figure 1c and SI Figure S2) using optical permittivities from the literature^{17–20} show that the long-wavelength plasmonic coupled mode for all three polymer-coated eNPoMs will blue-shift upon oxidation. This is confirmed by the experimental DF scattering spectra measured vs applied potential (Figure 2c). The oxidation of PANI gives a coupled-mode peak wavelength shift from around 645 to 578 nm, for PEDOT from 670 to 635 nm, and for PPy from 630 to 610 nm. Highly stable and reversible optical switching is observed (Figure 2d). Both PPy and PEDOT tune over narrower wavelength ranges than PANI, making their color dynamics harder to recognize by eye from their DF images (Figure 2b and SI Figure S4). Although not as good as Au@PANI in color dynamics for display applications,^{5,6} Au@PPy and Au@PEDOT have been used in switching devices^{21,22} as their absorption varies with their different redox states. Further FDTD simulations from different nanostructure configurations show the NPoM geometry gives consistent near-field enhancements in the gap, providing reliability for quantitative analysis of these polymers (SI Figure S3).

Polymer Redox Mechanism. To understand the charge transfer process during polymer redox, the recorded cyclic

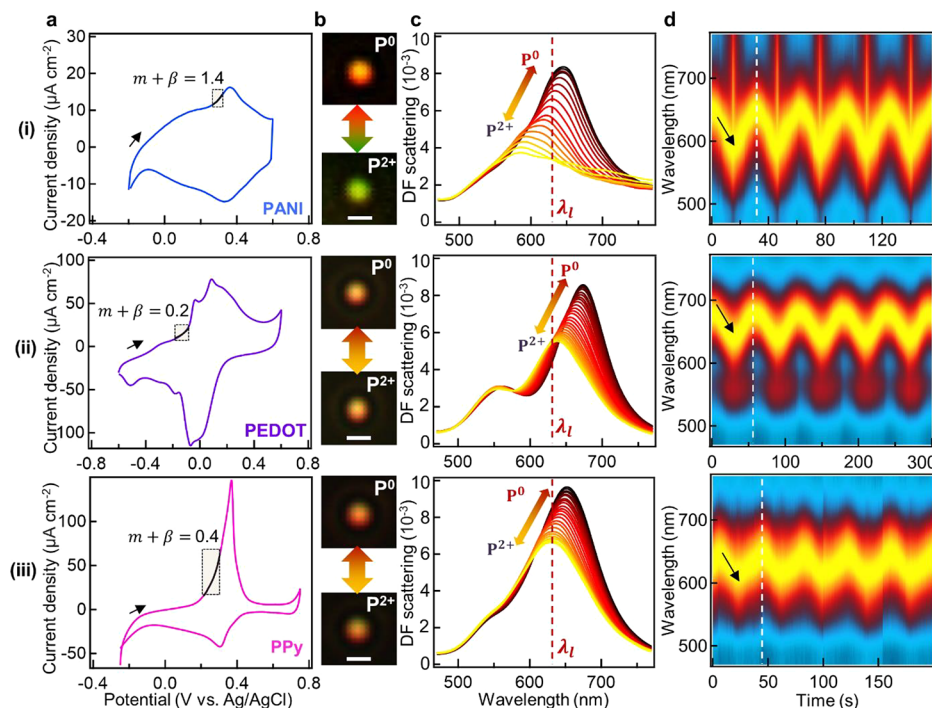
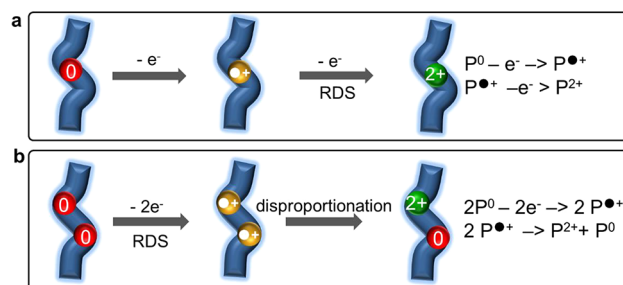


Figure 2. Optical switching of eNPMs. (i) Au@PANI for ramped voltages $-0.2 \leftrightarrow 0.6$ V, (ii) Au@PEDOT for $-0.6 \leftrightarrow 0.6$ V, and (iii) Au@PPy for $-0.25 \leftrightarrow 0.75$ V. (a) Cyclic voltammetry (CV) with apparent transfer coefficients ($m + \beta$, see background non-Faradaic capacitive current in SI Figure S5, and Tafel plots in Figure S6) ranging from 0 to 2, showing the transition state is reactant-like (P⁰) or product-like (P²⁺). Scan rate 50 mV s⁻¹. (b) Dark-field (DF) scattering images, scale bar 1 μm. (c) DF scattering spectra of single eNPMs as potential applied. Dashed $\lambda_l = 633$ nm is laser wavelength used for surface-enhanced Raman spectroscopy (SERS, see below). (d) Time-series normalized DF scattering spectra from single eNPMs over 5 cycles.

voltammetry (CV, Figure 2a) is analyzed in two respects. Thermodynamically, only one voltametric peak is observed for the $2e^-$ process in all three polymers, showing the potentials for the two electronic transitions are “potential inverted”,²³ i.e., oxidation of P^{•+} is easier than oxidation of P⁰. Note this also applies to Au@PEDOT, although a set of small prepeaks at ~ -0.2 V are observed due to the strongly trapped/released dopant counterions.^{7,24} Whether the P^{•+} intermediate is then observable will be governed by the rate of electron transfer (i.e., kinetics). Kinetically, the oxidative current is then plotted on a log scale (SI Figure S6, Tafel analysis²⁵) to determine the transfer coefficients ($m + \beta$). For a multielectron transfer process, it is possible to extract from Tafel plots an apparent transfer coefficient to determine the rate-determining step.^{23,25,26} Prior to this Tafel analysis, a background correction is used to remove the non-Faradaic contribution to the current from capacitance (SI Figure S5). The local potential in the NPM gap has been previously calibrated by the vibrational Stark effect.¹³ This shows that after non-Faradaic capacitive charging, the potential drops efficiently within 1 nm from the electrode surface, so Faradaic electron transfer happens readily between the Au mirror and molecular layer.

The apparent transfer coefficients are indicators for the rate-determining step (RDS), which is the $(m + 1)^{\text{th}}$ electron transfer. As $(m + \beta) = 1.4$ for PANI, the second electron loss is the RDS (i.e., oxidation of P^{•+}). By contrast, $(m + \beta) = 0.2$ for PEDOT and 0.4 for PPy, showing the first electron loss is the RDS (i.e., oxidation of P⁰). Two different types of electron-transfer mechanism thus occur during the redox transition (Scheme 1). For PANI, predominantly consecutive two-electron loss takes place stepwise, so all three redox states

Scheme 1. Mechanism of Conductive Polymer Redox^a



^aTwo pathways for oxidative doping: (a) Consecutive two-step electron transfer: $P^0 \rightarrow P^{\bullet+} \rightarrow P^{2+}$ by losing two electrons step-wise. (b) Disproportionation-type electron transfer: $P^0 \rightarrow P^{\bullet+}$ by losing one electron; then two P^{•+} rapidly combine to form a P²⁺ without extra electron transfers. RDS: rate-determining step.

should be observed during the reaction. For PEDOT and PPy, after the first electron loss, P^{•+} quickly combines with another P^{•+} and disproportionates into P²⁺ and P⁰,²⁶ so the P^{•+} intermediate is not observable.

Disproportionation becomes favorable when no extra energy is required to drive further electron transfer, and the process is triggered when the P^{•+} intermediate is stabilized.²⁶ Since electrons are more easily delocalized in PEDOT^{•+} and PPy^{•+} which possess more resonance structures (SI Figure S7a), they are more stable than PANI^{•+}. This is also reflected in the conductivity of $\sim 10^3$ S cm⁻¹ for PEDOT^{•+} and PPy^{•+}, which is much higher than that for PANI^{•+} of ~ 30 S cm⁻¹.²⁷ The lower conductivity of PANI is also evidenced by the higher capacitive background in CV (Figure 2a and SI Figure S5).

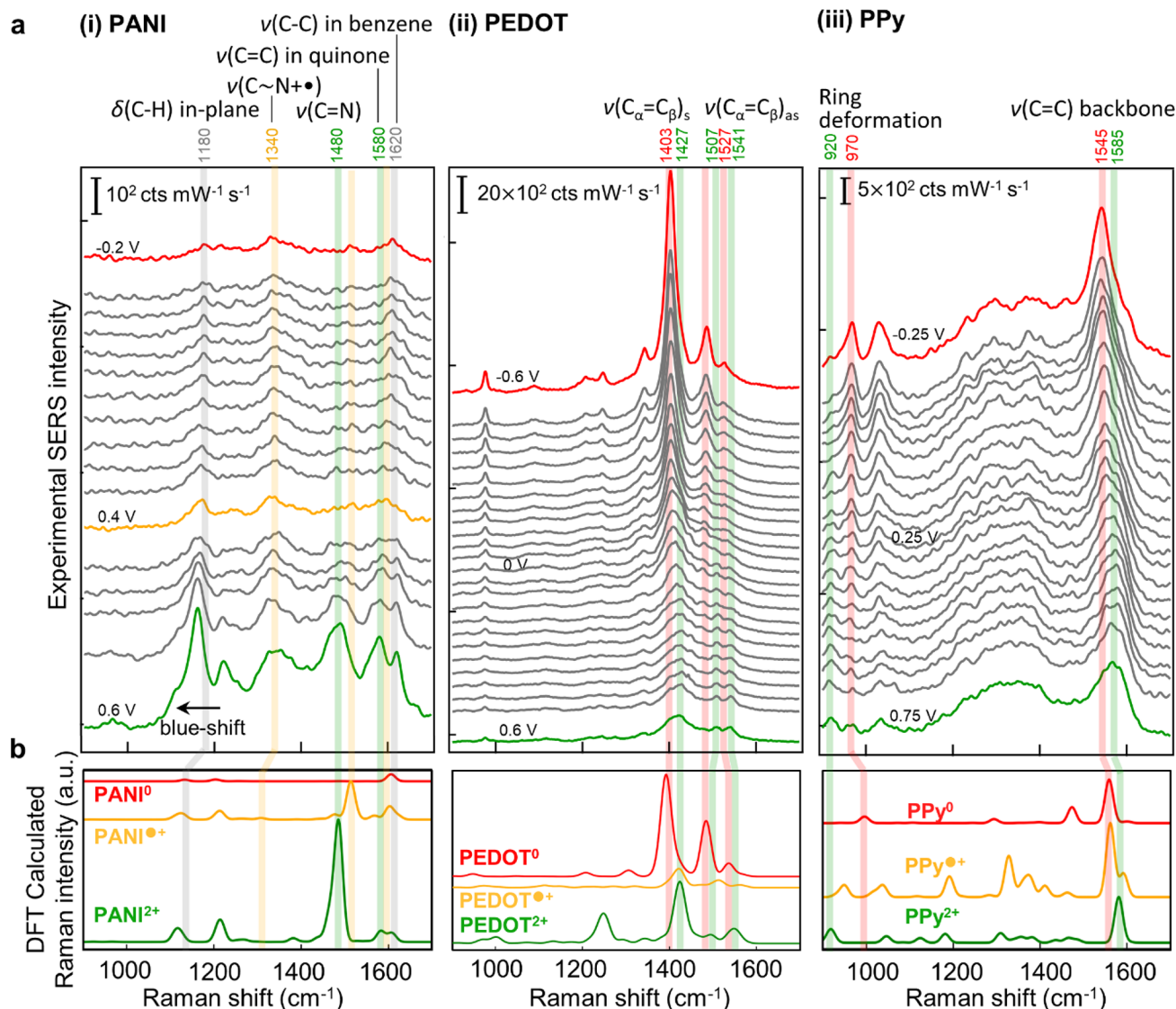


Figure 3. Raman evolution during redox. (a) Experimental SERS spectra vs voltage (top to bottom) as in Figure 2a. (b) DFT calculated Raman spectra. Red: P⁰, orange: P^{•+}, green: P²⁺. Vibrational modes relevant to oxidation are highlighted in orange and green; persistent modes of reduced state highlighted in red; modes seen in all three redox states are highlighted in gray.

Therefore, the disproportionation-type mechanism seems to predominate in more conductive polymers, while stepwise electron transfer prevails in less conductive polymers.

Tracking Dynamics and Detecting Reaction Intermediates. To examine further the polymer redox mechanism suggested by electrochemical measurements, *in situ* SERS spectra are recorded in real time vs applied potentials for the three eNPoM types (Figure 3a). The results are all comparable on different eNPoMs of the same type, showing consistency in the polymer shell coating and gap sizes. A 633 nm laser is used to provide efficiently outcoupled SERS spectra tuned near the plasmon resonance (Figure 2c), with a high signal-to-noise ratio using 1 s integration times for low powers of 100 μ W (see Methods). We note higher powers easily induce photochemical changes of metal and molecule. DFT Raman calculations are performed to simulate the SERS bands for the three polymers in different redox states (Figure 3b). Comparison of computational spectra with experimental SERS facilitates assignment of distinct SERS bands to corresponding vibrational modes (see top of Figure 3a, SI Table S1). Compared to reference

literature where polymers were studied in bulk, the main peaks observed here arise from polymers confined in plasmonic hotspots and show slight blue-shifts of a few cm⁻¹, indicating that the polymers are possibly more crystalline or have longer conjugation lengths than their bulk counterparts,^{28–30} offering an interesting scope for future study on polymer morphology (see below).

For PANI (Figure 3a (i)), three sets of SERS band changes are distinguished during the redox cycle. First, a set of bands at 1340 and 1480 cm⁻¹ are associated with $\nu(\text{C}-\text{N}^{\bullet+})$ and $\nu(\text{C}=\text{N})$, respectively. While the latter is characteristic for PANI²⁺, the former arises from an intermediate bond (resonant between a single and a double bond, see SI Figure S7a i) linked to the protonated nitrogen atoms in PANI^{•+}.^{31,32} Spectroscopic observation of PANI^{•+} aligns with the mechanism where consecutive two-step electron transfer occurs (see above, Scheme 1a). Second, a set of bands at 1580 and 1620 cm⁻¹ correspond respectively to $\nu(\text{C}=\text{C})$ in quinone rings from PANI²⁺, and $\nu(\text{C}-\text{C})$ in benzene rings from all three redox states. Extracting their intensities shows

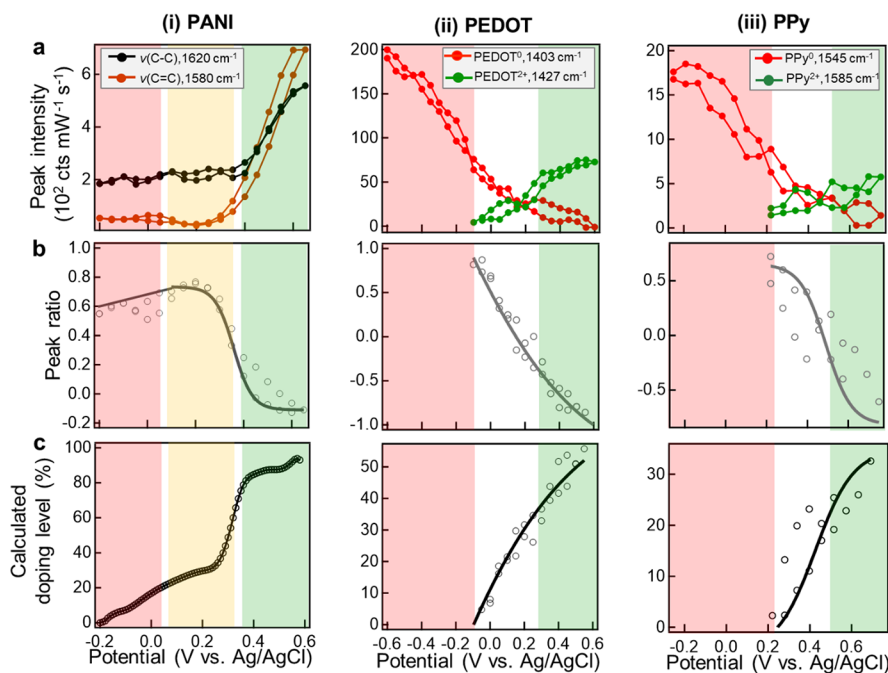


Figure 4. Analysis of SERS dynamics for tracking redox. (a) Extracted peak intensities vs applied potential of (i) $\nu(\text{C}-\text{C})$ at 1620 cm^{-1} and $\nu(\text{C}=\text{C})$ at 1580 cm^{-1} for PANI, (ii) symmetric $\nu(\text{C}_\alpha=\text{C}_\beta)$ for PEDOT⁰ at 1403 cm^{-1} and PEDOT²⁺ at 1427 cm^{-1} , and (iii) $\nu(\text{C}=\text{C})$ for PPy⁰ at 1545 cm^{-1} and PPy²⁺ at 1585 cm^{-1} . (b) Fractional ratio of the two components, defined as $(I_{\text{re}} - I_{\text{ox}})/(I_{\text{re}} + I_{\text{ox}})$ at each V. (c) Calculated doping level vs applied voltage. The red/yellow/green shaded regions correspond to the dominance of P⁰/P¹⁺/P²⁺ states from cyclic voltammograms in panel b, where region boundaries are defined by the onset and completion potentials of the oxidation peak. Solid lines are fits to sigmoid functions.

absolute changes of the two bands with voltage (Figure 4a (i)), while their intensity ratio shows how the redox processes compare to the cyclic voltammetry (Figure 4b (i)). Most evident is that the intensity of all SERS bands of PANI increases upon oxidation (Figure 4a (i) and SI Figure S8a), in contrast to PPy and PEDOT (Figure 4a (ii, iii), discussed below). This is attributed to the blue-shifting molecular absorption of PANI with oxidation from around 890 to 750 nm,³³ becoming closer to the excitation wavelength 633 nm, as well as the larger Raman cross sections given by the polarizable conjugated backbone from proton doping and dedoping (SI Figure S7b).³⁴ This enhances SERS emission from oxidized PANI which dominates the spectra and makes it hard to discern changes in reduced PANI. In contrast, the molecular absorption of PPy red-shifts from 360 to 490 nm with oxidation,³⁵ and PEDOT red-shifts from around 620 to 1600 nm with oxidation.³⁶ Use of shorter wavelength lasers (488 or 532 nm) might help the detection of the reduced species, but plasmonic heating by gold interband absorption damages polymers in the gap during continuous measurement.^{37,38} Third, the band at $\sim 1180\text{ cm}^{-1}$ is assignable to the in-plane $\delta(\text{C}-\text{H})$ associated with ring deformation throughout all three redox states. Although the intensity of this band is resonantly enhanced upon oxidation (SI Figure S8a), it also blue-shifts linearly with the applied potential (Figure S8b). Likely, $\delta(\text{C}-\text{H})$ does not track redox because it is a pendant mode away from the polymer chain and less influenced by charge variations on the backbone compared with the other modes discussed above.³²

For PEDOT (Figure 3ii), the most intense change in the SERS spectra is a band at 1403 cm^{-1} , which continuously broadens and red-shifts to 1427 cm^{-1} upon oxidation. These broad peaks are resolved into two components: the band at

1403 cm^{-1} is the symmetric $\nu(\text{C}_\alpha=\text{C}_\beta)$ from PEDOT⁰, and the other band at 1427 cm^{-1} is from PEDOT²⁺.^{39,40} According to analysis of these two components (Figure 4a (ii)), the band from PEDOT⁰ (red) initially dominates but decreases in intensity upon oxidation, with only $(5 \pm 5)\%$ remaining when oxidation is complete. Meanwhile, the band from PEDOT²⁺ (green) starts to appear at the onset potential around -0.1 V and shows the opposite trend increasing by $(74 \pm 16)\%$. Their ratio tracks the increasing proportion of PEDOT²⁺ to PEDOT⁰ (Figure 4b (ii)), directly indicating the oxidation level. The simultaneous observation of both bands at intermediate redox indicates the coexistence of PEDOT⁰ and PEDOT²⁺. The presence of both states is further confirmed by the splitting of the band at 1527 cm^{-1} into two bands at 1507 and 1541 cm^{-1} , associated with the asymmetric $\nu(\text{C}_\alpha=\text{C}_\beta)$ from PEDOT²⁺ and PEDOT⁰.^{41–43}

For PPy (Figure 3 (iii)), the most intense band is located at 1545 cm^{-1} , which broadens and red-shifts to 1585 cm^{-1} upon oxidation. This broad feature can again be decomposed into a pair of modes, assigned to the $\nu(\text{C}=\text{C})$ of the backbone from PPy⁰ and PPy²⁺, respectively.^{9,11} Peak intensity analysis (Figure 4a,b (iii)) shows the band from PPy⁰ decreases by $(67 \pm 15)\%$ upon oxidation, and the band from PPy²⁺ increases by $(40 \pm 22)\%$, demonstrating formation of PPy²⁺. Observation of both bands again implies that PPy⁰ and PPy²⁺ coexist. The same trend and coexistence are observed in another pair of bands at 970 and 920 cm^{-1} , assigned to the ring deformation modes from PPy⁰ and PPy²⁺, respectively (SI Figure S8c).

Comparing the SERS peak intensity changes for all three polymers (Figure 4a), it is obvious that PEDOT²⁺ and PPy²⁺ appear as soon as the potential hits the onset of oxidation (-0.1 V and $+0.2\text{ V}$) from the cyclic voltammograms (Figure 2a), while PANI²⁺ does not appear until the oxidation peak

potential (+0.4 V) is reached. This strongly confirms the two different mechanisms noted above: in the former case disproportionation-type oxidation occurs giving P^{2+} immediately at the onset potential, and in the latter case stepwise electron transfer takes place generating P^{2+} gradually upon complete oxidation. In addition, it is noticeable that PEDOT⁰ and PPy⁰ SERS intensities decrease even before the onset of oxidation (Figure 4a (ii,iii)). Rather than indicating a decrease in P^0 , this is likely due to changes of polymer polarizability resulting from the hydrogen evolution reaction (HER)⁴⁴ at negative potentials for the pH 2 solutions used. At positive potentials, no HER occurs, so SERS intensities can be directly correlated with P^0 concentration.

Estimation of Doping Levels. For PEDOT and PPy, analysis of SERS ratios can be used to estimate the proportion of reduced and oxidized states, and thus to estimate quantitatively the doping (oxidation) level (Figure 4c), which cannot be easily resolved from voltammograms. This calculation is less precise for PANI because of its electronic-resonance-enhanced response noted above (SI Figure S7b), resulting in dominant surface-enhanced resonance Raman scattering of PANI²⁺, but it is still provided as a rough estimation. Previous bulk Raman measurements on chemically doped PEDOT samples³⁹ have calibrated the ratio of the symmetric $\nu(C_\alpha=C_\beta)$ peaks to the doping level D ,

$$D (\%) \approx 12\% \ln(I_{\text{ox}}/I_{\text{re}}) + 29\% \quad (1)$$

where I_{ox} and I_{re} are intensities of P^{2+} and P^0 SERS bands respectively, and this applies in the voltage range when $I_{\text{ox}}/I_{\text{re}} > 1$. Using this calibration here suggests that the doping level of PEDOT increases from 0% at around -0.1 V to $\sim 50\%$ when electrochemical oxidation completes (Figure 4c (ii)). This doping level is significantly higher than the literature reported values of chemical doping in bulk of $<30\%$.³⁹ We suggest that this is due to the use of only a thin 20 nm polymer coating on the convex Au surface which facilitates dopant ion diffusion.⁴⁵ Assuming the backbone bonds in PPy (which are the same) follow the same doping dependence suggests that PPy doping increases to $(40 \pm 2)\%$ when oxidation completes (Figure 4c (iii)), which has not been previously measured. One reason for the lower final doping achieved could be that PPy is susceptible to oxygen from the ambient environment, so oxidative degradation competes with the doping process.^{46,47} By contrast PEDOT has excellent air stability and higher conductivity,⁴⁸ allowing for better switching and higher doping levels when oxidized. This accounts for the extensive use of PEDOT as a conductive material in applications.

The results show many subtle behaviors from polymer conformation and electrochemistry. For instance, additional effects are also observed when varying the polymer thickness and from choices of electrolyte.^{49–51} This enables many potential future directions to study how the polymer morphology, doping mechanism, polymer conductivity, and switching speed between different redox states, are influenced by different conditions. Intriguing prospects emerge when optical modes are further confined down to the sub-nm³ scale through “picocavities” formed by single adatoms, which can provide information on even single monomer redox events in a polymer chain. Such precision electrochemistry on the nanoscale is relevant to widespread applications, suggesting the approach shown here is of universal utility.

CONCLUSIONS

We have demonstrated the concept of eNPoMs with three different nanothick conjugated conductive polymers, PPy, PEDOT, and PANI. Highly reproducible optical switching is observed for each using dark-field spectroscopy in real time. *In-situ* SERS is measured in combination with cyclic voltammetry and compared with density functional theory calculations to reveal the different redox/doping mechanisms for polymers in the gap. For PANI, consecutive two-step electron transfer takes place, although the strong electronic resonance in the oxidized state interferes with measuring precise doping levels. For PPy and PEDOT, disproportionation-type electron transfer occurs so that after the first electron is lost, the polaron formed combines with the neighboring polarons to form a bipolaron. The type of redox/doping mechanism is found to be correlated with polymer conductivity. This work shows that it is possible to measure doping levels quantitatively in real time using vibrational changes of the C=C backbone, in sample volumes of only a few (10 nm)³ corresponding to only a few hundred unit cells.

METHODS

Polymer Coating on Gold Nanoparticles (Au NPs). The coating of all three conductive polymers on Au NPs used surfactant-assisted chemical oxidative polymerization methods.^{5,20,52} 1.6 mL of the citrate-stabilized Au NPs (BBI Solutions) solution is concentrated, followed by removal of the supernatant, and then mixing with the monomer solution and the surfactant (here, sodium dodecyl sulfate, SDS). The monomer molecules are attracted to the surface of the Au NPs due to electrostatic forces and the polymerization takes place upon adding oxidant (here, ammonium persulfate, APS).

For polypyrrole-coated Au NPs (Au@PPy) or poly-3,4-ethylenedioxythiophene-coated Au NPs (Au@PEDOT), the concentrated Au NPs solution is mixed with 0.78 mL of 10 mM pyrrole or 14.5 mM 3,4-ethylenedioxythiophene aqueous solution, together with 0.145 mL of 40 mM SDS. After vigorously vortexing, 0.69 mL of 19.1 mM APS is added with 8.25 μ L of 20 mM iron chloride (FeCl₃) solution. FeCl₃ acts as a catalyst here. For polyaniline-coated Au NPs (Au@PANI), 0.6 mL of 2 mM aniline is added to the Au NPs solution, together with 0.12 mL of 40 mM SDS, and then mixed with 0.6 mL of 2 mM APS in 10 mM hydrochloric acid (HCl). All these polymer-coated Au NPs solutions are incubated at room temperature overnight and then washed and redispersed in 4 mM SDS solution. The resulting polymer thickness is around 20 nm after incubation at room temperature overnight and can be controlled by adjusting the amount of monomer in each coating procedure or by repeating the whole coating process to deposit further layers.

Preparation of NPoM. Atomically smooth planar gold substrates are prepared by the template-stripping method as reported elsewhere.^{53,54} First, 100 nm-thick Au is evaporated onto a silicon wafer at a growth rate of 0.1 nm/s using an e-beam evaporator (Lesker LEV). Then, small pieces (*ca.* 1 cm²) of the bare Si wafer are glued on with epoxy and peeled off together with the Au layer. In the end, polymer-coated Au NPs are deposited by drop-casting the colloidal solution onto the Au substrates for 5 min, followed by distilled water rinsing and nitrogen gas drying. Before measurement, the samples are immersed in deionized water overnight to eliminate excess surfactants.

Electrochemical Cell. A fluid chamber is created by adhering two clean glass coverslips with a stack of center-removed square double-sided tape and filled with electrolyte solution (SI Figure S1). The electrolyte used for Au@PANI and Au@PPy is 0.5 M NaCl in 10 mM HCl, and for Au@PEDOT is 0.5 M NaCl aqueous solution. A low pH environment helps PANI and PPy mitigate the occurrence of irreversible overoxidation.^{55,56} The sample is sandwiched between the coverslips and immersed into the electrolyte. The Au layer substrate is used as the working electrode; the bare area is wired to a potentiostat (Autolab PGSTAT204, Metrohm). A Ag/AgCl reference

electrode (3 M KCl, eDAQ ET072, Green Leaf Scientific) and a platinum mesh counter electrode (Alfa Aesar) are inserted into the electrolyte, together with the Au working electrode to form a three-electrode configuration (SI Figure S1).

Scanning Electron Microscopic Analysis. Scanning electron microscopic (SEM) images of the samples are obtained using a LEO 1530VP (Zeiss) at an accelerating voltage of 10 kV.

Optical Imaging and Spectroscopy. Optical dark-field (DF) images and spectra of samples are acquired using a charge-coupled-device camera (Infinity 2) and spectrometer (Ocean Optics QE65000) with numerical aperture (NA) 0.8 100 \times objectives (Olympus LMPLFLN) in a customized microscope (Olympus BX51). A halogen lamp is used as the white light source. SERS measurements are recorded using the same microscope coupled to a 633 nm laser at 100 μ W with 1s integration time, and a 0.9 NA Olympus LWD objective for both excitation and collection. Spectra are recorded by an Andor Newton EMCCD camera coupled to a Horiba Triax 320 spectrometer.

Numerical Simulation. The electromagnetic response of the NPoM is simulated by finite-difference time-domain (FDTD) calculation software (Lumerical Solutions). The Au nanosphere surrounded with the spherical polymer shell is put onto a gold thin rectangular layer with specific thickness. The light is illuminated as a plane wave with desired polarization. The optical properties of gold and polymers are taken from the literature.^{17–20} To simplify the computation, the refractive index of the whole surrounding environment is set to $n = 1.33$ assuming water.

DFT Calculation. Polymers were modeled as a tetramer repeat unit to calculate the Raman spectra because only small changes in the HOMO and LUMO energy occur when using more repeat units.⁵⁷ Gas phase geometry optimizations and Raman frequency calculations were performed with no symmetry restrictions. B3LYP hybrid functional, def2svp basis set, and Grimme's D3 dispersion correction with Becke–Johnson damping were used.⁵⁸ To enhance the accuracy of calculations, the UltraFine integration grid was used. For PANI and PPy, TCheck was used to attempt to read a guess from the checkpoint file and to generate another one if necessary. The molecular geometry, charge, multiplicity, and title were read from the checkpoint file. If the first-order convergence method did not converge, it was switched to the second-order convergence method halfway through. For PANI, while complex proton-coupled electron transfer is involved in redox, calculations were able to confirm the protonation states at pH 2 (SI Figure S7c). For PEDOT, to obtain best-fit with experimental SERS for PEDOT, interaction with a gold atom is necessary in calculations (SI Figure S9), revealing that PEDOT provides coordination sites which are distinctive from the other two polymers. Tight convergence was used. The calculated SERS spectra were frequency scaled by factors of 0.94, 0.95, and 0.97 respectively for P⁰, P¹⁺, and P²⁺. Slightly different scaling factors were used because the difference in electron delocalization was not fully reflected in the calculations. All DFT calculations were carried out with the Gaussian 09 program package.⁵⁹

ASSOCIATED CONTENT

Data Availability Statement

All data for used for the figures is available upon reasonable request from the corresponding author.

Supporting Information

The Supporting Information is available free of charge at <https://pubs.acs.org/doi/10.1021/acsnano.2c09081>.

Schematic of the electrochemical cell; FDTD simulations of different eNPoMs; FDTD simulations of different nanostructure configurations; color dynamics comparison of different eNPoMs; schematics of non-Faradaic capacitive current and scan rate dependence measurement; electroanalysis of polymers; resonance structures and redox of different polymers; assignment of characteristic Raman bands; further analysis of SERS

dynamics during redox tracking; PEDOT tetramer-Au structure used in DFT for optimized SERS spectra and calculated UV–vis absorption spectra for PANI, PEDOT, and PPy (PDF)

AUTHOR INFORMATION

Corresponding Author

Jeremy J. Baumberg – NanoPhotonics Centre, Cavendish Laboratory, Department of Physics, University of Cambridge, Cambridge CB30HE, U.K.; orcid.org/0000-0002-9606-9488; Email: jjb12@cam.ac.uk

Authors

Jialong Peng – NanoPhotonics Centre, Cavendish Laboratory, Department of Physics, University of Cambridge, Cambridge CB30HE, U.K.; Present Address: (J.P.) College of Advanced Interdisciplinary Studies and Hunan Provincial Key Laboratory of Novel Nano-Optoelectronic Information Materials and Devices, National University of Defense Technology, Changsha 410073, China; orcid.org/0000-0002-3161-5855

Qianqi Lin – NanoPhotonics Centre, Cavendish Laboratory, Department of Physics, University of Cambridge, Cambridge CB30HE, U.K.; Present Address: (Q.L.) Hybrid Materials for Optoelectronics Group, Department of Molecules and Materials, MESA+ Institute for Nanotechnology and Center for Brain-Inspired Nano Systems, Faculty of Science and Technology, University of Twente, 7500 AE Enschede, The Netherlands; orcid.org/0000-0001-7578-838X

Tamás Földes – Department of Physics and Astronomy, University College London, London WC1E 6BT, U.K.; orcid.org/0000-0002-3978-1233

Hyeon-Ho Jeong – NanoPhotonics Centre, Cavendish Laboratory, Department of Physics, University of Cambridge, Cambridge CB30HE, U.K.; Present Address: (H.-H.J.) School of Electrical Engineering and Computer Science, Gwangju Institute of Science and Technology, Gwangju 61005, Republic of Korea; orcid.org/0000-0002-7029-9592

Yuling Xiong – NanoPhotonics Centre, Cavendish Laboratory, Department of Physics, University of Cambridge, Cambridge CB30HE, U.K.; orcid.org/0000-0003-1820-3722

Charalampos Pitsalidis – Department of Chemical Engineering and Biotechnology, University of Cambridge, Cambridge CB30AS, U.K.; Present Address: (C.P.) Department of Physics and Healthcare Engineering Innovation Center (HEIC), Khalifa University of Science and Technology, P.O. Box 127788, Abu Dhabi, UAE; orcid.org/0000-0003-3978-9865

George G. Malliaras – Electrical Engineering Division, Department of Engineering, University of Cambridge, Cambridge CB30FA, U.K.; orcid.org/0000-0002-4582-8501

Edina Rosta – Department of Physics and Astronomy, University College London, London WC1E 6BT, U.K.; orcid.org/0000-0002-9823-4766

Complete contact information is available at: <https://pubs.acs.org/doi/10.1021/acsnano.2c09081>

Author Contributions

[#]J.P. and Q.L. contributed equally. J.P., Q.L., H.-H.J., and J.J.B. conceived of and developed the experiments, together with J.P. who undertook the modeling, while Q.L. developed the electrochemistry aided by C.P. and G.G.M., and Q.L., T.F. and E.R. conducted the DFT calculations. All authors contributed to editing and critiquing the manuscript.

Notes

The authors declare no competing financial interest.

ACKNOWLEDGMENTS

We are grateful to B. de Nijs for support with fabrication, S. Hu for helping with SERS measurements, as well as the NanoPhotonics Centre and the Nanoscience Centre at the University of Cambridge for technical support. We acknowledge EPSRC grants (EP/N016920/1, EP/L027151/1, EP/T024550/1, EP/R013012/1, NanoDTC EP/L015978/1, EP/S022953/1), and ERC grants (project no. 883703 PICO-FORCE, 861950 POSEIDON, and 757850 BioNet). J.P. acknowledges the support from the National Natural Science Foundation of China (62105369). H.-H.J. acknowledges support from NRF grant (NRF-2021R1C1C1005060), DGIST R&D Program (21-IJRP-01), GIST Research Institute grant in 2021.

REFERENCES

- (1) Le, T. H.; Kim, Y.; Yoon, H. Electrical and Electrochemical Properties of Conducting Polymers. *Polymers* **2017**, *9* (4), 150.
- (2) Reese, C.; Roberts, M.; Ling, M.; Bao, Z. Organic Thin Film Transistors. *Mater. Today* **2004**, *7* (9), 20–27.
- (3) Wen, Y.; Liu, Y.; Guo, Y.; Yu, G.; Hu, W. Experimental Techniques for the Fabrication and Characterization of Organic Thin Films for Field-Effect Transistors. *Chem. Rev.* **2011**, *111* (5), 3358–3406.
- (4) Liao, C.; Yan, F. Organic Semiconductors in Organic Thin-Film Transistor-Based Chemical and Biological Sensors. *Polym. Rev.* **2013**, *53* (3), 352–406.
- (5) Peng, J.; Jeong, H. H.; Lin, Q.; Cormier, S.; Liang, H. L.; De Volder, M. F. L.; Vignolini, S.; Baumberg, J. J. Scalable Electrochromic Nanopixels Using Plasmonics. *Sci. Adv.* **2019**, *5* (5), 1–9.
- (6) Peng, J.; Jeong, H.-H.; Smith, M.; Chikkaraddy, R.; Lin, Q.; Liang, H.-L.; De Volder, M. F. L.; Vignolini, S.; Kar-Narayan, S.; Baumberg, J. J. Fully Printed Flexible Plasmonic Metafilms with Directional Color Dynamics. *Adv. Sci.* **2021**, *8* (2), 2002419.
- (7) Heinze, J.; Frontana-Urbe, B. A.; Ludwigs, S. Electrochemistry of Conducting Polymers—Persistent Models and New Concepts. *Chem. Rev.* **2010**, *110* (8), 4724–4771.
- (8) Bredas, J. L.; Street, G. B. Polarons, Bipolarons, and Solitons in Conducting Polymers. *Acc. Chem. Res.* **1985**, *18* (10), 309–315.
- (9) Liu, Y. C.; Hwang, B. J.; Jian, W. J.; Santhanam, R. In Situ Cyclic Voltammetry-Surface-Enhanced Raman Spectroscopy: Studies on the Doping-Undoping of Polypyrrole Film. *Thin Solid Films* **2000**, *374* (1), 85–91.
- (10) Santos, M. J. L.; Brolo, A. G.; Girotto, E. M. Study of Polaron and Bipolaron States in Polypyrrole by in Situ Raman Spectroelectrochemistry. *Electrochim. Acta* **2007**, *52* (20), 6141–6145.
- (11) Hou, Y.; Zhang, L.; Chen, L. Y.; Liu, P.; Hirata, A.; Chen, M. W. Raman Characterization of Pseudocapacitive Behavior of Polypyrrole on Nanoporous Gold. *Phys. Chem. Chem. Phys.* **2014**, *16* (8), 3523–3528.
- (12) Huang, H.; Karlsson, C.; Mamedov, F.; Strømme, M.; Gogoll, A.; Sjödin, M. Polaron Disproportionation Charge Transport in a Conducting Redox Polymer. *J. Phys. Chem. C* **2017**, *121* (24), 13078–13083.
- (13) Wright, D.; Lin, Q.; Berta, D.; Földes, T.; Wagner, A.; Griffiths, J.; Readman, C.; Rosta, E.; Reisner, E.; Baumberg, J. J. Mechanistic

Study of an Immobilized Molecular Electrocatalyst by in Situ Gap-Plasmon-Assisted Spectro-Electrochemistry. *Nat. Catal.* **2021**, *4* (2), 157–163.

(14) Stec, G. J.; Lauchner, A.; Cui, Y.; Nordlander, P.; Halas, N. J. Multicolor Electrochromic Devices Based on Molecular Plasmonics. *ACS Nano* **2017**, *11* (3), 3254–3261.

(15) Grady, N. K.; Halas, N. J.; Nordlander, P. Influence of Dielectric Function Properties on the Optical Response of Plasmon Resonant Metallic Nanoparticles. *Chem. Phys. Lett.* **2004**, *399*, 167.

(16) Kristensen, A.; Yang, J. K. W.; Bozhevolnyi, S. I.; Link, S.; Nordlander, P.; Halas, N. J.; Mortensen, N. A. Plasmonic Colour Generation. *Nat. Rev. Mater.* **2017**, *2* (1), 16088.

(17) Johnson, P. B.; Christy, R. W. Optical Constants of the Noble Metals. *Phys. Rev. B* **1972**, *6* (12), 4370–4379.

(18) Barbero, C.; Kotz, R. Nanoscale Dimensional Changes and Optical Properties of Polyaniline Measured by In Situ Spectroscopic Ellipsometry. *J. Electrochem. Soc.* **1994**, *141* (4), 859–865.

(19) Kim, Y. T.; Allara, D. L.; Collins, R. W.; Vedam, K. Real-Time Spectroscopic Ellipsometry Study of Theelectrochemical Deposition of Polypyrrole Thin Films. *Thin Solid Films* **1990**, *193–194* (PART 1), 350–360.

(20) Zhou, J.; Panikkanvalappil, S. R.; Kang, S.; Yu, S.; Zhang, S.; El-Sayed, M.; Tsukruk, V. V. Enhanced Electrochemical Dark-Field Scattering Modulation on a Single Hybrid Core-Shell Nanostructure. *J. Phys. Chem. C* **2019**, *123* (46), 28343–28352.

(21) Xiong, K.; Emilsson, G.; Maziz, A.; Yang, X.; Shao, L.; Jager, E. W. H.; Dahlin, A. B. Plasmonic Metasurfaces with Conjugated Polymers for Flexible Electronic Paper in Color. *Adv. Mater.* **2016**, *28* (45), 9956–9960.

(22) Xiong, K.; Tordera, D.; Emilsson, G.; Olsson, O.; Linderhed, U.; Jonsson, M. P.; Dahlin, A. B. Switchable Plasmonic Metasurfaces with High Chromaticity Containing Only Abundant Metals. *Nano Lett.* **2017**, *17* (11), 7033–7039.

(23) Batchelor-McAuley, C.; Compton, R. G. Voltammetry of Multi-Electron Electrode Processes of Organic Species. *J. Electroanal. Chem.* **2012**, *669*, 73–81.

(24) Hillman, A. R.; Daisley, S. J.; Bruckenstein, S. Ion and Solvent Transfers and Trapping Phenomena during N-Doping of PEDOT Films. *Electrochim. Acta* **2008**, *53* (11), 3763–3771.

(25) Compton, R. G.; Banks, C. E. Electrode Kinetics. In *Understanding Voltammetry*; Compton, R. G.; Banks, C. E. World Scientific Publishing Europe: London, 2018; pp 37–82.

(26) Lin, Q.; Li, Q.; Batchelor-McAuley, C.; Compton, R. G. Two-Electron, Two-Proton Oxidation of Catechol: Kinetics and Apparent Catalysis. *J. Phys. Chem. C* **2015**, *119* (3), 1489–1495.

(27) Balint, R.; Cassidy, N. J.; Cartmell, S. H. Conductive Polymers: Towards a Smart Biomaterial for Tissue Engineering. *Acta Biomater.* **2014**, *10* (6), 2341–2353.

(28) Wen, P.; Tan, C.; Zhang, J.; Meng, F.; Jiang, L.; Sun, Y.; Chen, X. Chemically Tunable Photoresponse of Ultrathin Polypyrrole. *Nanoscale* **2017**, *9* (23), 7760–7764.

(29) Nightingale, J.; Wade, J.; Moia, D.; Nelson, J.; Kim, J. S. Impact of Molecular Order on Polaron Formation in Conjugated Polymers. *J. Phys. Chem. C* **2018**, *122* (51), 29129–29140.

(30) Tsoi, W. C.; James, D. T.; Kim, J. S.; Nicholson, P. G.; Murphy, C. E.; Bradley, D. D. C.; Nelson, J.; Kim, J. S. The Nature of In-Plane Skeleton Raman Modes of P3HT and Their Correlation to the Degree of Molecular Order in P3HT:PCBM Blend Thin Films. *J. Am. Chem. Soc.* **2011**, *133* (25), 9834–9843.

(31) Mažeikienė, R.; Niaura, G.; Malinauskas, A. Raman Spectroelectrochemical Study of Polyaniline at UV, Blue, and Green Laser Line Excitation in Solutions of Different PH. *Synth. Met.* **2018**, *243*, 97–106.

(32) Bernard, M. C.; Hugot-Le Goff, A. Quantitative Characterization of Polyaniline Films Using Raman Spectroscopy. I: Polaron Lattice and Bipolaron. *Electrochim. Acta* **2006**, *52* (2), 595–603.

(33) Malinauskas, A.; Holze, R. Cyclic UV-Vis Spectroelectrochemistry of Polyaniline. *Synth. Met.* **1998**, *97* (1), 31–36.

- (34) Mažeikienė, R.; Niaura, G.; Malinauskas, A. Study of Redox and Protonation Processes of Polyaniline by the Differential Multiwavelength Raman Spectroelectrochemistry. *Spectrochim. Acta - Part A Mol. Biomol. Spectrosc.* **2019**, *221* (4), 117147.
- (35) Arjomandi, J.; Shah, A. U. H. A.; Bilal, S.; Van Hoang, H.; Holze, R. In Situ Raman and UV-Vis Spectroscopic Studies of Polypyrrole and Poly(Pyrrole-2,6-Dimethyl- β -Cyclodextrin). *Spectrochimica Acta - Part A: Molecular and Biomolecular Spectroscopy*. **2011**, *78* (1), 1–6.
- (36) Gribkova, O. L.; Iakobson, O. D.; Nekrasov, A. A.; Cabanova, V. A.; Tverskoy, V. A.; Tameev, A. R.; Vannikov, A. V. Ultraviolet-Visible-Near Infrared and Raman Spectroelectrochemistry of Poly(3,4-Ethylenedioxythiophene) Complexes with Sulfonated Polyelectrolytes. The Role of Inter- and Intra-Molecular Interactions in Polyelectrolyte. *Electrochim. Acta* **2016**, *222*, 409–420.
- (37) Inouye, H.; Tanaka, K.; Tanahashi, I.; Hirao, K. Ultrafast Dynamics of Nonequilibrium Electrons in a Gold Nanoparticle System. *Phys. Rev. B - Condens. Matter Mater. Phys.* **1998**, *57* (18), 11334–11340.
- (38) Baffou, G.; Quidant, R. Thermo-Plasmonics: Using Metallic Nanostructures as Nano-Sources of Heat. *Laser Photonics Rev.* **2013**, *7* (2), 171–187.
- (39) Chiu, W. W.; Travaš-Sejdić, J.; Cooney, R. P.; Bowmaker, G. A. Spectroscopic and Conductivity Studies of Doping in Chemically Synthesized Poly(3,4-Ethylenedioxythiophene). *Synth. Met.* **2005**, *155* (1), 80–88.
- (40) Augusto, T.; Teixeira Neto, É.; Teixeira Neto, Â. A.; Vichessi, R.; Vidotti, M.; De Torresi, S. I. C. Electrophoretic Deposition of Au@PEDOT Nanoparticles towards the Construction of High-Performance Electrochromic Electrodes. *Sol. Energy Mater. Sol. Cells* **2013**, *118*, 72–80.
- (41) Savva, A.; Wustoni, S.; Inal, S. Ionic-to-Electronic Coupling Efficiency in PEDOT:PSS Films Operated in Aqueous Electrolytes. *J. Mater. Chem. C* **2018**, *6* (44), 12023–12030.
- (42) Garreau, S.; Louarn, G.; Buisson, J. P.; Froyer, G.; Lefrant, S. In Situ Spectroelectrochemical Raman Studies of Poly(3,4-Ethylenedioxythiophene) (PEDT). *Macromolecules* **1999**, *32* (20), 6807–6812.
- (43) Kulandaivalu, S.; Zainal, Z.; Sulaiman, Y. Influence of Monomer Concentration on the Morphologies and Electrochemical Properties of PEDOT, PANI, and PPy Prepared from Aqueous Solution. *Int. J. Polym. Sci.* **2016**, *2016*, 1–12.
- (44) Di Martino, G.; Turek, V. A.; Lombardi, A.; Szabó, I.; De Nijs, B.; Kuhn, A.; Rosta, E.; Baumberg, J. J. Tracking Nanoelectrochemistry Using Individual Plasmonic Nanocavities. *Nano Lett.* **2017**, *17* (8), 4840–4845.
- (45) Xiong, K.; Olsson, O.; Svirelis, J.; Palasingh, C.; Baumberg, J.; Dahlin, A. Video Speed Switching of Plasmonic Structural Colors with High Contrast and Superior Lifetime. *Adv. Mater.* **2021**, *33* (41), 2103217.
- (46) Thiéblemont, J. C.; Brun, A.; Marty, J.; Planche, M. F.; Calo, P. Thermal Analysis of Polypyrrole Oxidation in Air. *Polymer (Guildf)*. **1995**, *36* (8), 1605–1610.
- (47) Uyar, T.; Toppare, L.; Hacaloğlu, J. Spectroscopic Investigation of Oxidation of P-Toluene Sulfonic Acid Doped Polypyrrole. *Synth. Met.* **2001**, *123* (2), 335–342.
- (48) Gueye, M. N.; Carella, A.; Faure-Vincent, J.; Demadrille, R.; Simonato, J. P. Progress in Understanding Structure and Transport Properties of PEDOT-Based Materials: A Critical Review. *Progress in Materials Science*. **2020**, *108*, 100616.
- (49) Chiu, W. W.; Travaš-Sejdić, J.; Cooney, R. P.; Bowmaker, G. A. Studies of Dopant Effects in Poly(3,4-Ethylenedioxythiophene) Using Raman Spectroscopy. *J. Raman Spectrosc.* **2006**, *37* (12), 1354–1361.
- (50) Lacroix, J. C.; Kanazawa, K. K.; Diaz, A. Polyaniline: A Very Fast Electrochromic Material. *J. Electrochem. Soc.* **1989**, *136* (5), 1308.
- (51) Camurlu, P. Polypyrrole Derivatives for Electrochromic Applications. *RSC Adv.* **2014**, *4* (99), 55832–55845.
- (52) Xing, S.; Tan, L. H.; Yang, M.; Pan, M.; Lv, Y.; Tang, Q.; Yang, Y.; Chen, H. Highly Controlled Core/Shell Structures: Tunable Conductive Polymer Shells on Gold Nanoparticles and Nanochains. *J. Mater. Chem.* **2009**, *19* (20), 3286–3291.
- (53) Benz, F.; Chikkaraddy, R.; Salmon, A.; Ohadi, H.; De Nijs, B.; Mertens, J.; Carnegie, C.; Bowman, R. W.; Baumberg, J. J. SERS of Individual Nanoparticles on a Mirror: Size Does Matter, but so Does Shape. *J. Phys. Chem. Lett.* **2016**, *7* (12), 2264–2269.
- (54) Hegner, M.; Wagner, P.; Semenza, G. Ultralarge Atomically Flat Template-Stripped Au Surfaces for Scanning Probe Microscopy. *Surf. Sci.* **1993**, *291* (1–2), 39–46.
- (55) Pei, Q.; Qian, R. Protonation and Deprotonation of Polypyrrole Chain in Aqueous Solutions. *Synth. Met.* **1991**, *45* (1), 35–48.
- (56) Li, Y.; Qian, R. Electrochemical Overoxidation of Conducting Polypyrrole Nitrate Film in Aqueous Solutions. *Electrochim. Acta* **2000**, *45* (11), 1727–1731.
- (57) McCormick, T. M.; Bridges, C. R.; Carrera, E. I.; DiCarmine, P. M.; Gibson, G. L.; Hollinger, J.; Kozycz, L. M.; Seferos, D. S. Conjugated Polymers: Evaluating DFT Methods for More Accurate Orbital Energy Modeling. *Macromolecules* **2013**, *46* (10), 3879–3886.
- (58) Grimme, S.; Ehrlich, S.; Goerigk, L. Effect of the Damping Function in Dispersion Corrected Density Functional Theory. *J. Comput. Chem.* **2011**, *32* (7), 1456–1465.
- (59) Frisch, M. J.; Trucks, G. W.; Schlegel, H. B.; Scuseria, G. E.; Robb, M. A.; Cheeseman, J. R.; Scalmani, G.; Barone, V.; Mennucci, B.; Petersson, G. A.; Nakatsuji, H.; Caricato, M.; Li, X.; Hratchian, H. P.; Izmaylov, A. F.; Bloino, J.; Zheng, G.; Sonnenberg, J. L.; Hada, M.; Ehara, M.; et al. *Gaussian 09*, Revision E; Gaussian, Inc.: Wallington, CT, 2009.